Journal of Cleaner Production 239 (2019) 117873

Contents lists available at ScienceDirect

Journal of Cleaner Production

journal homepage: www.elsevier.com/locate/jclepro

Carbothermal reduction for preparing nZVI/BC to extract uranium: Insight into the iron species dependent uranium adsorption behavior

Huimin Zhang [a], Yang Ruan [a], Aiping Liang [a], Kaimin Shih [b], Zenghui Diao [c], Minhua Su [a], Li'an Hou [a], Diyun Chen [a], Hui Lu [d], Lingjun Kong [a, b, *]

[a] Guangdong Provincial Key Laboratory of Radionuclides Pollution Control and Resources, School of Environmental Science and Engineering, Guangzhou University, Guangzhou, 510006, China
[b] Department of Civil Engineering, The University of Hong Kong, Pokfulam Road, Hong Kong, PR China
[c] School of Environmental Science and Engineering, Zhongkai University of Agriculture and Engineering, Guangzhou, 510225, China
[d] School of Environmental Science and Engineering, Sun Yat-sen University, Guangzhou, 510275, China

ARTICLE INFO

Article history:
Received 8 June 2019
Received in revised form
7 July 2019
Accepted 1 August 2019
Available online 2 August 2019

Handling Editor: Baoshan Huang

Keywords:
Nano-zero valent iron
Biochar
Carbothermal reduction
Uranium

ABSTRACT

Currently, a lot of uranium containing wastewater was generated in China, which required efficient treatment before being discharged. Immobilization of uranium on ZVI has attracted many concerns from researchers in the world wide. Surface oxidation and agglomeration limited the efficiency of nano zero-valent iron (nZVI) in remediation of uranium pollution. In this work, a green carbothermal reduction process was conducted to prepare environmental friendly biochar-supported ZVI (nZVI/BC). Immobilization behavior of uranium on nZVI/Cs, oxidized nZVI/Cs and Fe_3O_4 from wastewater were investigated. The iron salt was converted into iron oxides at 700 °C, further being reduced into nZVI in the presence of ferric chloride and ferric nitrate being carbonization of starch at 800 and 900 °C. The uranium adsorption capacities were different from the carbonization temperature and iron sources, which depended on the transformation of iron species. The maximum adsorption capacities of nano-flake Fe_{Cl}/C (1:4–900) and nanoparticles Fe_N/C (1:4–900) for U(VI) were 34.82 and 55.14 mg/g. The removal efficiencies of Fe_{Cl}/C (1:4–900) and nanoparticles Fe_N/C (1:4–900) were higher than that of 44% for C–Fe_3O_4. The SEM-mapping and XPS analysis of nZVI/Cs after U(VI) adsorption indicated that the immobilization of U(VI) was ascribed to simultaneous adsorption and reduction.

© 2019 Elsevier Ltd. All rights reserved.

1. Introduction

There is an increase in the discharge of uranium containing wastewater with the rapid development of nuclear industry and the overexploitation of uranium. Efficient treatment methods were required to control the uranium pollution to human health (X.M. Wu et al., 2019). To the best of our knowledge, adsorption is one of the efficient methods for removing heavy metal ions such as uranium from wastewater (Xie et al., 2019a, b). Nanomaterials were widely concerned on removing heavy metal ions (Y.H. Wu et al., 2019). Fortunately, uranium in wastewater could be efficiently removed by various nanomaterials (Huang et al., 2019; Wang et al., 2019a. b) and metal organic frameworks (Li et al., 2018; Xie et al., 2019a, b). Besides, nano-zero-valent iron (nZVI) is also widely used in uranium decontamination. In 1995, Cantrell et al. proposed that ZVI could be used to remove uranium (U) from wastewater. The concentration of uranium was decreased from 450 to 2 μg/L by ZVI, but the removal mechanism was not highlighted (Cantrell et al., 1995). Thereafter, the effective treatment of radioactive uranium-containing wastewater by ZVI has been given more and more attention. Crane et al. compared the effect of nZVI and nano-magnetite (nFe_3O_4) on removing uranium (Crane et al., 2011). The experimental results showed that the removal efficiency of U(VI) by nZVI reached 98% within 2 h, and the residual concentration of U(VI) remained stable for 48 h. However, ZVI nanoparticles tended to be aggregated and were easily oxidized in the air (Ryu et al., 2011; Phenrat et al., 2007), which greatly limited the application of nZVI in wastewater pollution remediation. Supporting of nZVI on porous supporters could avoid the oxidation and aggregation of nZVI particles. Supporters such as silica microspheres (Qiu et al.,

* Corresponding author. Guangdong Provincial Key Laboratory of Radionuclides Pollution Control and Resources, School of Environmental Science and Engineering, Guangzhou University, Guangzhou, 510006, China.
E-mail address: kongljun@gzhu.edu.cn (L. Kong).

https://doi.org/10.1016/j.jclepro.2019.117873
0959-6526/© 2019 Elsevier Ltd. All rights reserved.

2011), clay minerals (Zhang et al., 2010; Diao et al., 2016), polyacrylamide (Ling et al., 2015), metal oxides (Mangal et al., 2013), and carbon materials (Messele et al., 2014; Wang et al., 2019a. b) had attracted much attention. Commonly, carbon supported nZVI were well known since the carbon had high surface area and pore volume (Yan et al., 2015).

Generally, the carbon supported nZVI materials were prepared by liquid phase reduction with sodium borohydride ($NaBH_4$) (Sun et al., 2014; Jing et al., 2015) and plasma technique (Li et al., 2015). Nevertheless, toxic reagents were used in this process, and by-products (boric acid) would cause secondary pollution (Lv et al., 2019).

Fortunately, nano-flake ZVI was found in the carbonized Fe-rich sludge at a temperature of 800 °C in our previously work (Kong et al., 2016). Moreover, it was found that the coke oven gas promoted the reduction of iron oxide into zero-valent iron in the blast furnace smelting (Chen et al., 2015). In these cases, not only the production of ZVI was observed during carbothermal reduction, but also the produced ZVI was loaded on the biochar. It is believed that carbothermal reduction is green and clean for ZVI/C synthesis, in which the volatiles released from the carbonization of biomass played an important role in the reduction process (Chen et al., 2015). However, our previous study found that FeS was observed by carbothermal reduction with a mixture of ferrous sulfate ($FeSO_4$) and flour under nitrogen atmosphere (Kong et al., 2018). The formation of ZVI may be dependent on the type of iron salts in carbothermal reduction process. It is urgently needed to investigate the transformation of Fe during carbothermal reduction process for understanding the application of ZVI in uranium immobilization. Herein, carbothermal reduction for synthesis of ZVI/C was reported, in which the starch was used as biomass. The effect of iron sources on ZVI transformation in carbothermal reduction was investigated. The uranium immobilization behavior dependent on the transformation of iron species was understood.

In this work, nZVI/C composites were synthesized by carbonizing the mixture of different types of salts (ferric sulfate, ferric chloride, and ferric nitrate) and starch with various mass ratios at different temperatures (700, 800, 900 °C) under nitrogen atmosphere. The nZVI/C were characterized by X-ray diffraction (XRD), scanning electron microscope (SEM), and X-ray photoelectron spectroscopy (XPS) to understand the transformation of iron species. Batch adsorption experiments were conducted to evaluate the U(VI) immobilization behavior. Coupling reduction and adsorption of U(VI) on nZVI/C was hypothesized and confirmed by SEM-mapping and XPS analysis. Thus, the immobilization behavior of uranium dependent on iron species was investigated to understand the carbothermal synthesis of nZVI/C and its application in U(VI) decontamination.

2. Materials and experiments

2.1. Materials

Ferric sulfate ($Fe_2(SO_4)_3$), ferric chloride ($FeCl_3\cdot 6H_2O$), ferric nitrate ($Fe(NO_3)_3\cdot 9H_2O$), starch were all of analytical reagent grade, being purchased from Aladdin Bio-Chem Technology Co., Ltd (Shanghai, China). 1 g/L of U(VI) stock solution was prepared from uranyl nitrate ($UO_2(NO_3)_2\cdot 6H_2O$) (GR) for subsequent experiments. All solutions were prepared with ultrapure water.

2.2. Synthesis of nZVI/C

ZVI/C was prepared by carbothermal reduction process in this study. First, iron salts ($Fe_2(SO_4)_3$, $FeCl_3\cdot 6H_2O$, $Fe(NO_3)_3\cdot 9H_2O$) and starch were thoroughly stirred in ultrapure water, where the mass ratio of iron to starch was 1:2.5, 1:4 and 1:8. Next, the mixtures were placed in a vacuum oven and dried at 80 °C to obtain the iron-containing precursors. Subsequently, the obtained different precursors with different ratio were filled into the ceramic arks and then placed in a quartz tube of the programmed tube electrical furnace (LTKC-5-12, China). After the nitrogen (N_2) was involved into the tube to sweep the remained air, the precursors were carbonized at 700, 800, and 900 °C for 2 h, with a heating rate of 5 °C/min. Finally, the obtained samples were sieved through the 150 meshes sieve after being cooled to room temperature. The samples were named as Fe_S/C (1:n-T),Fe_{Cl}/C (1:n-T), and Fe_N/C (1:n-T), where the letter "T" represented the carbonization temperature, "S", "Cl", and "N" represented $Fe_2(SO_4)_3$, $FeCl_3\cdot 6H_2O$, $Fe(NO_3)_3\cdot 9H_2O$, and "1:n" was the mass ratio of iron to starch, respectively. Moreover, starch was firstly carbonized at 900 °C under N_2 atmosphere, and then the pre-carbonized starch char was mixed with $FeCl_3$ and $Fe(NO_3)_3$ at the mass ratio of Fe to starch of 1:4. After the mixtures were dried, they were carbonized again at 900 °C. The obtained samples were named as Fe_{Cl}/C-900 and Fe_N/C-900, respectively.

2.3. Batch adsorption experiments

Batch adsorption experiments of U(VI) ($C_0 = 20$ mg/L) by the ZVI/C were carried out in a series of conical flasks. To investigate the adsorption characteristics, a determined mass of Fe/C_{Cl}(1:4—900) and Fe/C_N(1:4—900) were poured into 50 mL U(VI) solution. The solution pH values were adjusted with 0.1 M HNO_3 and 0.1 M KOH, and then the flasks were placed in a digital thermostatic water bath oscillator (SHA-82A, China) at 30 °C. 5 mL of mixture was taken out at the determined time interval and filtered through a filtration membrane to remove the suspended sorbent. The residual U(VI) concentration in the filtrate was measured by a UV-Fluorescence uranium analyzer (WGJ-III, China) reported by Han et al., (2018). The adsorption capacities (q_t, mg/g) and removal efficiency (R, %) of U(VI) by ZVI/C at "t" time could be calculated by the following equations:

$$q_t = \frac{(C_0 - C_t) \times V}{m} \quad (1)$$

$$\mathrm{R} = \frac{C_0 - C_t}{C_0} \times 100\% \quad (2)$$

Where C_0 (mg/L) is the initial concentration of the U(VI) solution, C_t (mg/L) and q_t (mg/g) are the residual concentration and adsorption amount at t time (min), m (g) is the mass of the sample, V(L) represents the volume of the U(VI) solution, and R (%) is the removal efficiency.

2.4. Analytical methods

The XRD patterns were recorded with Cu Kα at 40 kV and 40 mA in the range of 5-80° by using a powder X-ray diffractometer (PW3040/60, PANalytical, Holland). The surface morphology and mapping analysis were both conducted by a scanning electron microscope (JED-2300, JEOL, Japan). The specific surface area (S_{BET}) and pore size distribution were determined with an auto-adsorption system (ASAP 2460, America) at 77K through a nitrogen adsorption-desorption method. The functional groups on the surface of the material were identified and analyzed with a Fourier-transform infrared spectrometer (TENSOR II Hyperion, 2000; Bruker, Germany) at a wavelength of 400—4000 cm^{-1}. The XPS spectra of samples before and after adsorption were conducted by using an electron spectrometer (Thermo Escalab 250). The charge distribution on the surface of ZVI/C was measured by a zeta

potential meter (90 plus Zeta, America).

3. Results and discussion

3.1. Characterization of ZVI/C

Since the ZVI could be obtained at 900 °C by carbothermal reduction using bioorganic matter as a carbon source (Kong et al., 2016), Fig. S1 presented the corresponding XRD patterns of the Fe/Cs by carbonizing the precursors with different iron salts at 900 °C. Clearly, diffraction peaks located at 44.7° and 65° were observed for Fe_{Cl}/C (1:4–900) and Fe_N/C (1:4–900), which were assigned to ZVI, indicating the presence of ZVI in Fe_{Cl}/C (1:4–900) and Fe_N/C (1:4–900) after carbothermal reduction at 900 °C. However, pyrrhotite ($Fe_{(1-x)}S$) rather than ZVI peak was found in Fe_S/C (1:4–900) when the $Fe_2(SO_4)_3$ was used as iron source. Although the carbonization temperature is one of the key factors determining the formation of ZVI, the production of Fe was different from the iron salts, indicating that the iron salt types had a critical effect on the formation of ZVI. To further understand the production of ZVI during the carbothermal reduction, Fe_{Cl}/C-900 and Fe_N/C-900 were prepared by carbonizing the mixtures of pre-carbonized starch char with $Fe(NO_3)_3$ and $FeCl_3$. The XRD patterns were presented in Fig. S1 comparatively. Interestingly, diffraction peaks being assigned to ZVI were observed in Fe_N/C-900, while the ZVI peak in Fe_{Cl}/C was inconspicuous. It is well known that many volatiles were released from carbonization of starch into char. These volatiles could provide a reducing atmosphere, favoring the reduction of Fe^{3+} into ZVI. It could be explained by the fact that the reducing gas, which was volatilized during the carbonization process, promoting the formation of ZVI in Fe_{Cl}/C (1:4–900). Moreover, ZVI was also observed in Fe_N/C-900 although the starch carbon was a substitute of starch. It is easy to understand that starch carbon was beneficial to the formation of ZVI when the iron salt was $Fe(NO_3)_3$. The starch char may play an important role in carbothermal reduction for synthesis of ZVI.

The SEM images of Fe_{Cl}/C (1:4–900) and Fe_N/C (1:4–900) were clearly shown in Fig. 1(a and b) to understand their micro-

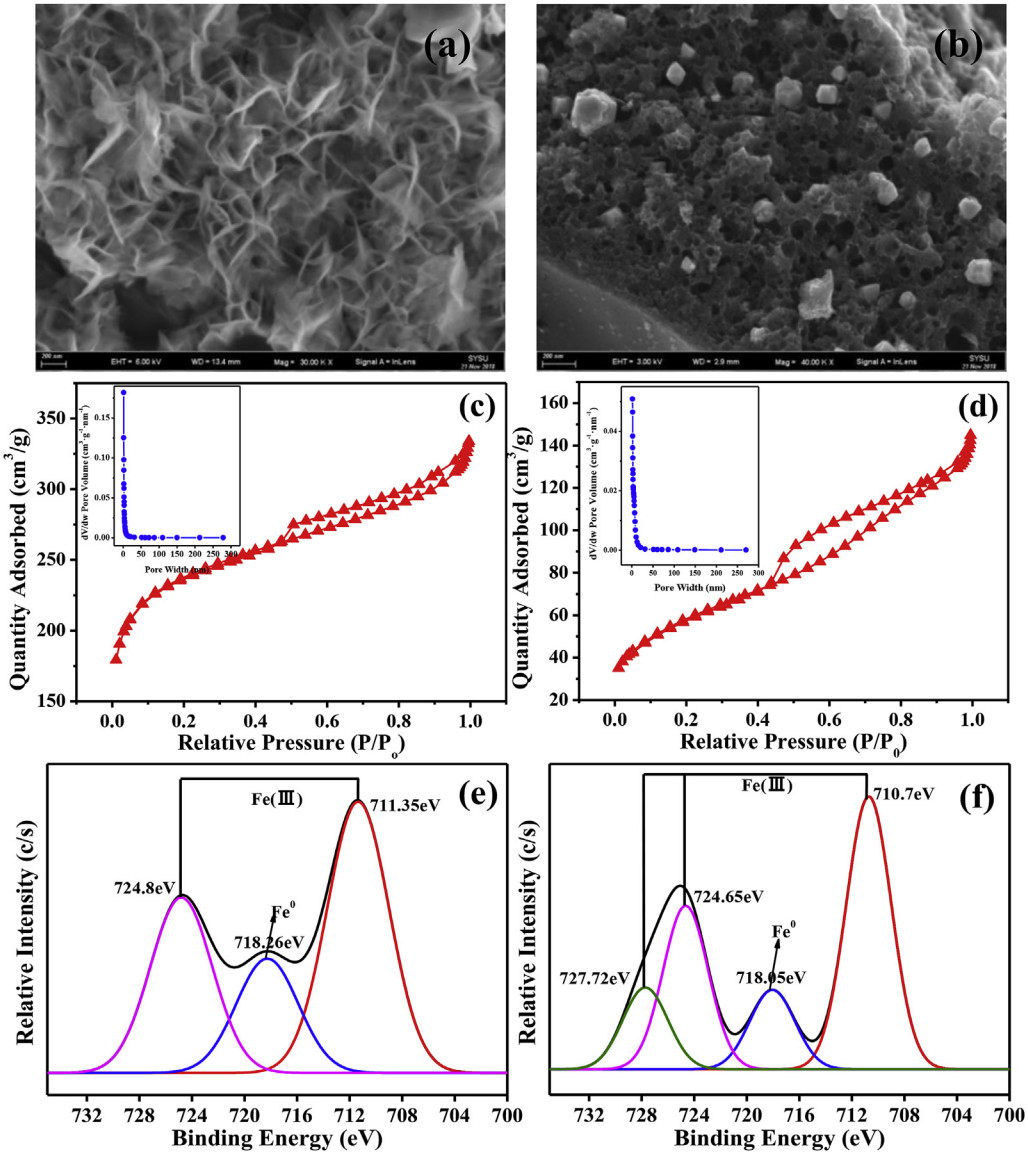


Fig. 1. SEM images of Fe_{Cl}/C (1:4–900) (a) and Fe_N/C (1:4–900) (b); the N_2 adsorption/desorption isotherms of Fe_{Cl}/C (1:4–900) (c) and Fe_N/C (1:4–900) (d) (the insets represent the pore size distributions); The narrow scan XPS spectra of Fe 2p for Fe_{Cl}/C (1:4–900) (e) and Fe_N/C (1:4–900) (f).

morphology. Evidently, the ZVI in Fe_{Cl}/C (1:4–900) performed nanosheets, while the ZVI performed nanoparticles in Fe_N/C (1:4–900), and these ZVI nanoparticles were embedded in the carbon layer. The specific surface areas of Fe_{Cl}/Cs and Fe_N/Cs were shown in Table 1, in which the S_{BET} of Fe_{Cl}/C (1:4–900) and Fe_N/C (1:4–900) were 782.05 and 204.85 m^2/g, respectively. Simultaneously, the specific surface areas increased with the starch content in Fe_{Cl}/Cs and Fe_N/Cs, and the surface area values of Fe_{Cl}/Cs were greater than those of Fe_N/Cs. The results could be explained by the fact that the $FeCl_3$ might play a preferable role in the activation of starch char to $FeNO_3$ since the $ZnCl_2$ was widely used as an activator to enhance the surface area of activated carbon (Qian et al., 2007). The N_2 adsorption/desorption isotherms of Fe_{Cl}/C (1:4–900) and Fe_N/C (1:4–900) were investigated in Fig. 1(c and d), and the pore size distributions were measured using the BJH method. The average pore size was 3.6 nm for Fe_{Cl}/C (1:4–900) and 4.6 nm for Fe_N/C (1:4–900), respectively. The narrow scan XPS spectra of Fe 2p peaks in Fe_{Cl}/C (1:4–900) and Fe_N/C (1:4–900) were illustrated in Fig. 1(e and f). The peaks located at 718.26 and 718.05 eV were identified as Fe (0) 2p. In addition, peaks located at 711.35 and 710.7 eV were attributed to Fe2p 3/2, and peaks fixed at 724.8, 724.65, and 727.72 eV were determined to Fe 2p 1/2, all of which were combined with "O" element. The FT-IR spectra of Fe_{Cl}/C (1:4–900) and Fe_N/C (1:4–900) were displayed in Fig. S3. The C–O adsorption band appeared at 1652 cm^{-1} (Hu et al., 2019). The peaks at 2361, 2349, 1793, 1560, and 699 cm^{-1} were relevant to stretching vibrations of the C=O bonds (Liu et al., 2017), and the peak at 565 cm^{-1} was assigned to Fe–O group (Song et al., 2014). FT-IR analysis indicated that the presence of abundant oxygen-containing functional groups provided more adsorption sites for U(VI).

3.2. Adsorption studies

The pH value of the aqueous solution greatly influenced the U(VI) adsorption because it seriously affected the U(VI) species in the solution (Misaelides et al., 1995; Chen et al., 2017; Han et al., 2018). Fig. 2(a) showed that the U(VI) adsorption by Fe_{Cl}/C (1:4–900) increased markedly from pH value of 3–7, where the highest removal efficiency was 93.1% at pH value of 7. After that, the U(VI) adsorption by Fe_{Cl}/C (1:4–900) significantly decreased. The surface charge potentials of Fe_{Cl}/C (1:4–900) were displayed in Fig. 2(b), the zero point charge value (pH_{zpc}) of Fe_{Cl}/C (1:4–900) was 7.14, which was consistent with the pH value with the optimal removal efficiency. Moreover, the adsorption behavior of Fe_N/C (1:4–900) to U(VI) was very similar to that of Fe_{Cl}/C (1:4–900) with the change of pH value. As the pH value rose from 3 to 6, the removal efficiency of U(VI) by Fe_N/C (1:4–900) sharply increased to 94.3% at pH value of 6. Furthermore, the U(VI) removal efficiencies by Fe_N/C (1:4–900) decreased as the increase in the pH value, which may be ascribed to the fact that the pH_{zpc} value of Fe_N/C (1:4–900) was 6.81. It is noteworthy that the pH value affects the relative distribution of U(VI) species (Zhu et al., 2018). UO_2^{2+}, UO_2OH^+, $(UO_2)_2(OH)_2^{2+}$ and $(UO_2)_3(OH)_5^+$ were observed when the pH value was lower than 6, all of them were positively charged (Zhu et al., 2018; Chen et al., 2017). The surface of Fe_{Cl}/C (1:4–900) and Fe_N/C (1:4–900) were both positive charged when the pH was lower than their pH_{zpc} values as shown in Fig. 2(b). The electrostatic repulsion force between the adsorbents and the positive charged U(VI) species resulted in the unfavorable adsorption of positive charged U(VI). The positive potential decreased as the pH value increase to about 7. The electrostatic repulsion force was weakened, resulting in the increase in the removal efficiencies of U(VI) when the pH value increased from 3 to 7. The U(VI) removal efficiencies on Fe_{Cl}/C (1:4–900) and Fe_N/C (1:4–900) were the highest when the pH value ranged from 6 to 7. In this case, $[(UO_2)_3(OH)_5]^+$, $[UO_2(OH)]^+$ and $UO_2(OH)_2$ were observed (Qian et al., 2015), the electrostatic repulsion force was negligible. When the solution pH value increased to higher than the pH_{zpc}, the surface charge of adsorbent was negative. Also, three species of $UO_2(OH)_2$, anion species $[UO_2(OH)_3]^-$ and $[(UO_2)_3(OH)_7]^-$ were the major species when the solution pH was higher than 8 (Qian et al., 2015; Liu et al., 2016). The same negative charges of adsorbents and U(VI) species led to the electrostatic repulsion and unfavorable adsorption of U(VI), which was consistent with the decreased removal efficiency of U(VI) as the pH value increased. In this case, the electrostatic repulsion force also increased as the increase in the solution pH value, resulting in the decrease in the U(VI) removal efficiencies. The above results suggested that electrostatic repulsion force could not contribute to U(VI) removal by Fe_N/C (1:4–900) and Fe_{Cl}/C (1:4–900) at the solution pH value of 6 and 7. In addition, the

Table 1
BET surface areas of Fe_{Cl}/Cs and Fe_N/Cs.

Samples	S_{BET} (m^2/g)
Fe_{Cl}/C (1:2.5–900)	550.39
Fe_{Cl}/C (1:4–900)	782.05
Fe_{Cl}/C (1:8–900)	1016.70
Fe_N/C (1:2.5–900)	25.01
Fe_N/C (1:4–900)	204.85
Fe_N/C (1:8–900)	374.30

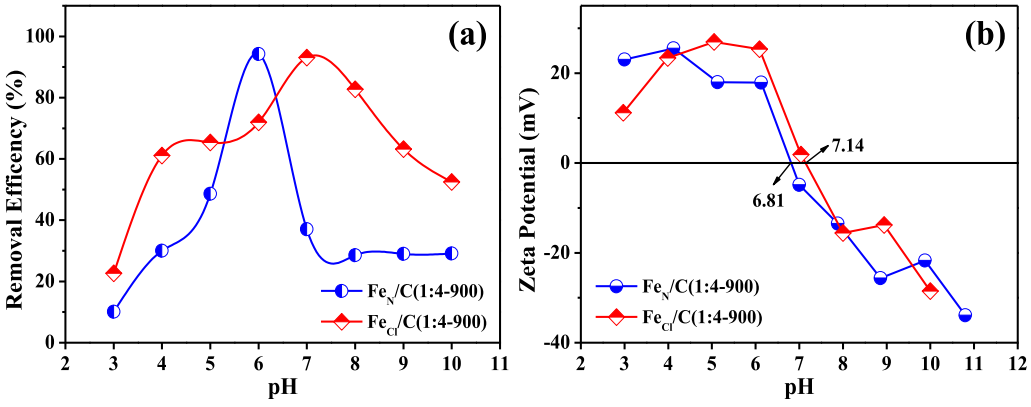


Fig. 2. (a) Effect of pH value on the sorption of U(VI) with Fe/Cs; (b) Zeta potential versus different pH for Fe/Cs (C_0: 20 mg/L, dosage: 2 g/L of Fe_{Cl}/C (1:4–900) and 1 g/L of Fe_N/C (1:4–900), T: 30 °C).

subsequent experiments would be carried out at the solution pH of 6 for Fe_N/C (1:4–900) and 7 for Fe_{Cl}/C (1:4–900).

The optimal dosage of Fe_N/C (1:4–900) and Fe_{Cl}/C (1:4–900) during uranium adsorption was investigated at Fig. S4. The dosage of Fe_{Cl}/C (1:4–900) highly influenced the uranium removal efficiencies. The removal efficiencies increased to about 95% in the dosage of 2 g/L of Fe_{Cl}/C (1:4–900) and the dosage of 1 g/L of Fe_N/C (1:4–900). To explicitly analyze the adsorption behavior of Fe_{Cl}/Cs to U(VI), the adsorption properties of the adsorbents obtained at various carbonization temperatures and mass ratios of Fe to starch were firstly considered in Fig. 3. The removal efficiency (83.9%) of Fe_{Cl}/C (1:2.5–900) for U(VI) was lower than that 96.6% of Fe_{Cl}/C (1:4–900), which had been shown in Fig. 3(a). Since ZVI had favorable effect on uranium immobilization (Lv et al., 2019), while Fe_3O_4 and ZVI were observed in Fe_{Cl}/C (1:2.5–900) and only ZVI was observed for Fe_{Cl}/C (1:4–900) as shown in Fig. S2(a). The discrepancy in the removal efficiencies of Fe_{Cl}/C (1:4–900) and Fe_{Cl}/C (1:2.5–900) might be ascribed to the fact that the pure ZVI was observed in Fe_{Cl}/C (1:4–900) but Fe_{Cl}/C (1:2.5–900) was not. The difference between the two adsorbents was mainly due to that the content of biochar in Fe_{Cl}/C (1:2.5–900) was not enough to convert Fe_3O_4 into ZVI. Strangely, the main components of Fe_{Cl}/C (1:4–900) and Fe_{Cl}/C (1:8–900) were both ZVI, but the removal efficiency of U(VI) by Fe_{Cl}/C (1:8–900) was only 76.6%, being lower than that of Fe_{Cl}/C (1:4–900). The above situation was mainly explained by the higher biochar and lower ZVI content in Fe_{Cl}/C (1:8–900). The results were also seen from Fig. 3(c) for Fe_N/Cs. The order of removal efficiency of U(VI) by Fe_N/Cs was: Fe_N/C (1:4–900) (96.4%) >Fe_N/C (1:8–900) (71.5%) > Fe_N/C (1:2.5–900) (35.4%). Since the component in Fe_N/C (1:2.5–900) were iron oxides instead of ZVI as displayed in Fig. S2(c), its adsorption capacity was lower than those of Fe_N/C (1:4–900) and Fe_N/C (1:8–900). What is more, the U(VI) adsorption capacity of Fe_N/C (1:8–900) was less than that of Fe_N/C (1:4–900) as the mass ratio of Fe to starch changed from 1:8 to 1:4, it could be explained by the decreased ZVI content in Fe_N/C (1:8–900).

Furthermore, the adsorption performances of U(VI) by Fe_{Cl}/Cs and Fe_N/Cs carbonized at different temperatures were also investigated in Fig. 3(b) and (d). Obviously, as the carbonization temperature raised from 700 to 900 °C, the order of U(VI) removal efficiencies by Fe_{Cl}/Cs was: Fe_{Cl}/C (1:4–900) (96.6%) > Fe_{Cl}/C (1:4–800) (62.9%) > Fe_{Cl}/C (1:4–700) (6.1%). What is interesting, Fe_{Cl}/C (1:4–900) showed more favorable adsorption ability while pure ZVI diffraction peak existed in both Fe_{Cl}/C (1:4–900) and Fe_{Cl}/C (1:4–800) as seen from the XRD analysis. It may be attributed to that Fe_{Cl}/C (1:4–800) was a transitional form of Fe_{Cl}/C (1:4–900), because the ZVI peak intensity of Fe_{Cl}/C (1:4–800) was weaker than that of Fe_{Cl}/C (1:4–900) as seen from Fig. S2(b). As the carbonization temperature decreased to 700 °C, there only Fe_3O_4 was observed (Fig. S2(b)), which led to the lowest uranium adsorption capacity. It could be explained by the fact that the iron presented as Fe_3O_4 was not preferable to uranium adsorption comparing to ZVI. As shown in Fig. 3(b), when the carbonization temperature was 700 and 800 °C, the U(VI) removal efficiencies of the Fe_N/C (1:4–700) and Fe_N/C (1:4–800) were very close (about 55%), which were greatly lower than that of Fe_N/C (1:4–900). ZVI was formed only when the carbonization temperature reached 900 °C in Fe_N/Cs as displayed in Fig. S2(d). These results illustrated that the existence of ZVI in Fe/Cs played a role in U(VI) adsorption. Also, the content of ZVI determined the adsorption behavior of U(VI) by Fe_{Cl}/Cs and Fe_N/Cs. In brief, the mass ratio of Fe to starch and carbonization temperature were crucial factors determining ZVI formation. Of course, the nZVI could be successfully obtained when the carbonization temperature reached 900 °C and mass ratio of Fe to starch was 1:4.

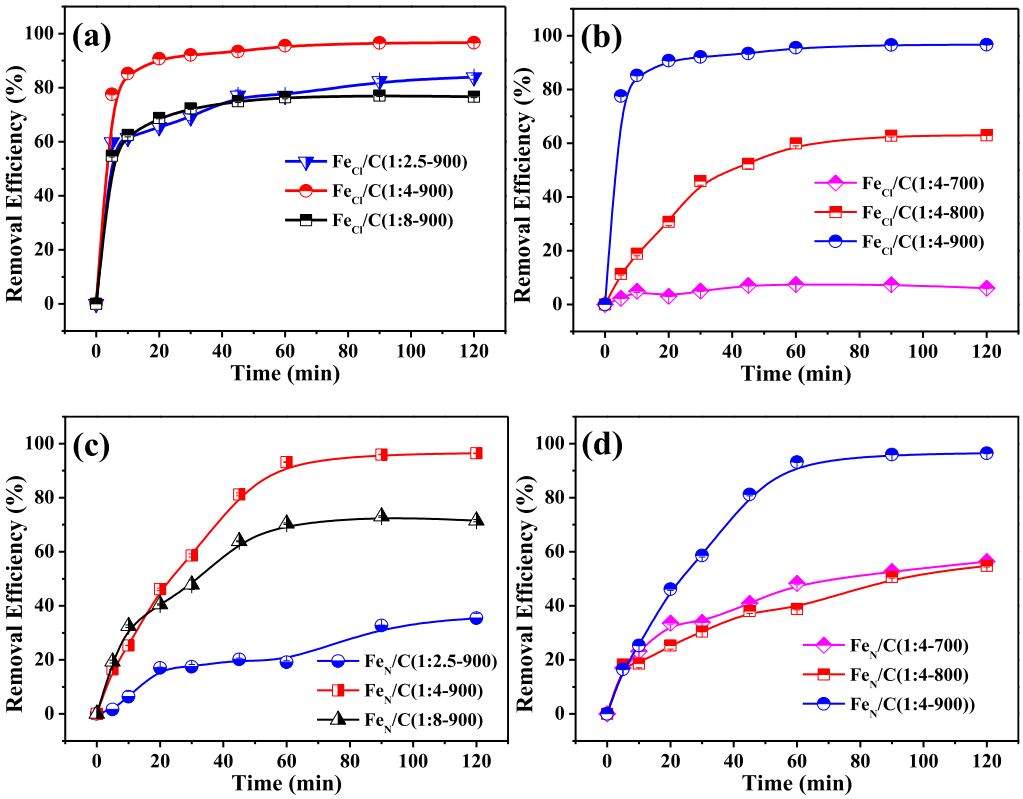


Fig. 3. The effect of mass ratio of iron to starch (a and c) and carbonization temperature (b and d) on U(VI) removal efficiencies by Fe_{Cl}/Cs and Fe_N/Cs (C_0: 20 mg/L, dosage: 2 g/L of Fe_{Cl}/Cs and 1 g/L of Fe_N/Cs, T: 30 °C).

The obtained nZVI/C performed the best ability to U(VI) adsorption from wastewater.

To further distinguish the role of the iron oxides and ZVI in the U(VI) adsorption, the products of Fe_{Cl}/C (1:8–900) and Fe_N/C (1:8–900), being oxidized in air at 60 °C for 7 days, were conducted for uranium adsorption comparatively. The U(VI) removal efficiency by oxidized Fe_{Cl}/C (1:8–900) decreased from 76.6 (Fig. 3(a)) to 70.8% (Fig. 4). Interestingly, the U(VI) removal efficiency of oxidized Fe_N/C (1:8–900) fell down to 29.3%, which was much lower than that of 71.5% for Fe_N/C (1:8–900) in Fig. 3(c). These results were mainly owing to that the ZVI was converted into iron oxides after being exposed in air condition. Thus, the content of ZVI in Fe_{Cl}/C (1:8–900) and Fe_N/C (1:8–900) decreased and the content of iron oxides increased. Their adsorption abilities were decreased as the decrease in the content of ZVI, further confirming that the oxidization of ZVI into iron oxides played an unfavorable role in U(VI) adsorption. Besides, adsorption of uranium on commercial Fe_3O_4 (C–Fe_3O_4) was also investigated to confirm the effect of nZVI in Fe_N/C (1:4–900) on uranium adsorption. As can be seen from Fig. 4, the removal efficiency of U(VI) by C–Fe_3O_4 only reached 44%, suggesting that Fe_3O_4 did not dominate the removal of U(VI) (Yang et al., 2018). This was consistent with the low removal efficiency of Fe_{Cl}/C (1:4–700) performed in the form of Fe_3O_4 as described above. Finally, the adsorption properties of Fe_S/C (1:4–900) were also compared. It could be found that the removal efficiencies of U(VI) on Fe_S/C (1:4–900) at pH 6 and 7 were 64.8% and 36.5%, respectively, which were much lower than those of Fe_N/C (1:4–900) and Fe_{Cl}/C (1:4–900). Fe_S/C (1:4–900) also showed weaker adsorption ability of U(VI) comparing with Fe_N/C (1:4–900) and Fe_{Cl}/C (1:4–900), which resulted from the fact that ZVI in Fe_N/C (1:4–900) and Fe_{Cl}/C (1:4–900) rather than $Fe_{(1-x)}S$ in Fe_S/C (1:4–900) played a major role in uranium adsorption. Thus, the apparent difference in U(VI) removal efficiencies was ZVI dependent reduction, being consistent with the reported ZVI/C (Wang et al., 2019a. b; Ling and Zhang, 2015). Above all, carbonization temperature, mass ratio of Fe to starch and the type of iron salts are the significant factors in carbothermal reduction progress determining the formation of ZVI, which highly influenced the U(VI) adsorption.

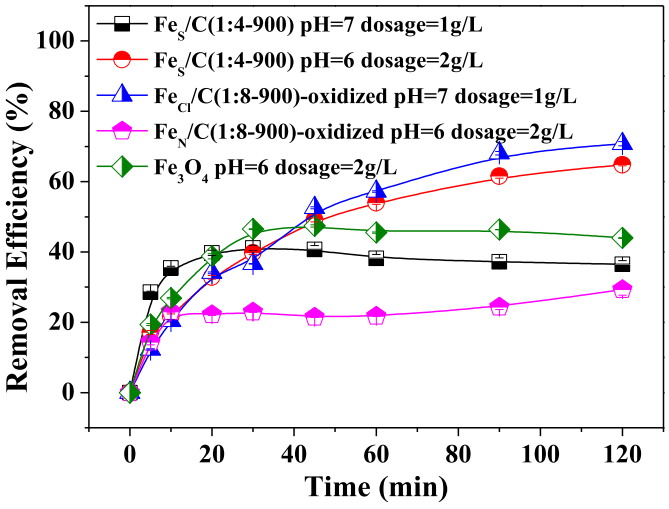


Fig. 4. The removal efficiencies of U(VI) by different adsorbents as a function of contact time (C_0: 20 mg/L, T: 30 °C).

The relationship between the equilibrium adsorption capacities of Fe_{Cl}/C (1:4–900) and Fe_N/C (1:4–900) for U(VI) and the equilibrium U(VI) concentration in solution was explained by adsorption isotherm. Two commonly used isothermal models (Langmuir and Freundlich) were used to describe the application of Fe_{Cl}/C (1:4–900) and Fe_N/C (1:4–900) in U(VI) adsorption. The nonlinear fitting curves of the Langmuir and Freundlich models are expressed by Eqs. (3) and (4), respectively.

$$q_e = \frac{q_m K_L C_e}{1 + K_L C_e} \tag{3}$$

$$q_e = K_F C_e^{1/n} \tag{4}$$

Where q_e and q_m (mg/g) are the equilibrium and maximum adsorption amounts on the surface of adsorbents, respectively; C_e is the equilibrium solution concentration (mg/L); and K_L (L/mg) and K_F [(mg/g)/(mg/L)^n] are the equilibrium constants of Langmuir and Freundlich, respectively; and n is the intensity parameter of Freundlich model.

The specific fitting information was listed in Fig. 5 (a) and Table 2. Apparently, the correlation coefficient (R^2) of Langmuir model for Fe_{Cl}/C (1:4–900) was 0.986, which was higher than the 0.882 of Freundlich model. The R^2 value of Langmuir model (0.970) was larger than the value of 0.886 for Freundlich model. The high correlation coefficient was consistent with the Langmuir model better, and the corresponding maximum adsorption capacities were 34.82 mg/g for Fe_{Cl}/C (1:4–900) and 55.14 mg/g for Fe_N/C (1:4–900), respectively, indicating that the adsorption of U(VI)

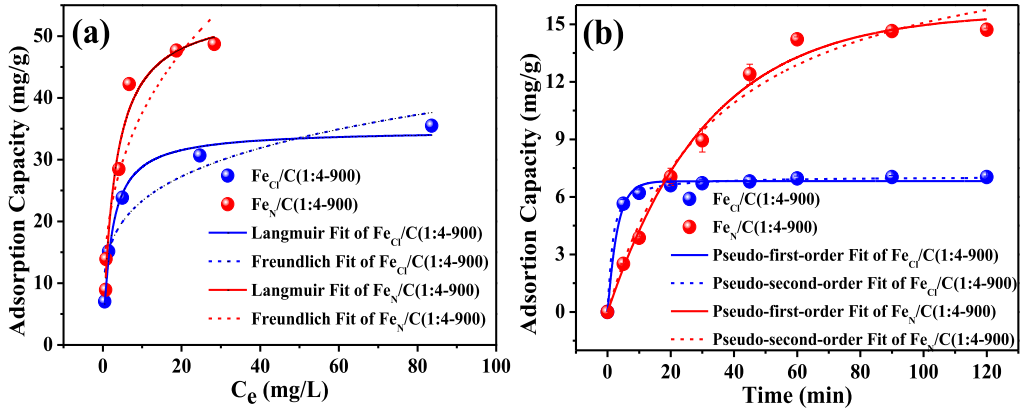


Fig. 5. (a) Adsorption isotherms plots of Fe_{Cl}/C (1:4–900) and Fe_N/C (1:4–900) fitted to Langmuir and Freundlich models. (b) Adsorption kinetics of Fe_{Cl}/C (1:4–900) and Fe_N/C (1:4–900) fitted to pseudo-first-order and pseudo-second-order models.

Table 2
Isothermal adsorption model parameters of Fe_{Cl}/C (1:4–900) and Fe_N/C (1:4–900) for U(VI).

Adsorbent	Langmuir			Freundlich		
	q_m (mg/g)	k_L (L/mg)	R^2	n	K_F (mg/g) (L/mg)$^{1/n}$	R^2
Fe_{Cl}/C (1:4–900)	34.82	0.48	0.986	4.43	13.88	0.882
Fe_N/C (1:4–900)	55.14	0.33	0.970	2.96	17.26	0.866

followed the monolayer adsorption.

The nonlinear fitted kinetic models (pseudo-first-order and pseudo-second-order) were also used to evaluate the adsorption behavior of U(VI) by Fe_{Cl}/C (1:4–900) and Fe_N/C (1:4–900). As shown in Eqs. (5) and (6), the kinetic data in Fig. 5(b) and the parameters in Table 3 were fitted by the nonlinear kinetic models:

$$q_t = q_e(1 - e^{k_1 t}) \tag{5}$$

$$q_t = \frac{k_2 q_e^2 t}{1 + k_2 q_e t} \tag{6}$$

Where k_1, k_2 represent the adsorption rate constants; q_t and q_e (mg/g) are the adsorption capacities at "t" time and at equilibrium, respectively.

In Fig. 5(b), the pseudo-second-order kinetic model fitted well with the experiment data of Fe_{Cl}/C (1:4–900) to U(VI), and the correlation coefficient was 0.999 as well as the calculated q_e was 7.06 mg/g. Therefore, the mechanism of U(VI) adsorption by Fe_{Cl}/C (1:4–900) was owing to chemisorption, and the main factor may be the reduction of ZVI.

3.3. Characterization of ZVI/C after uranium immobilization

Comparing with the photos before adsorption, the surface morphology of the two adsorbents changed significantly after adsorption of U(VI) as shown in Fig. 6(a) and (b). The nanosheet structure of Fe_{Cl}/C (1:4–900) got significantly thicker after uranium

Table 3
Nonlinear fitted pseudo-first-order and pseudo-second-order models of U(VI) adsorption on Fe_{Cl}/C (1:4–900) and Fe_N/C (1:4–900).

Sample	Pseudo-first-order			Pseudo-second-order		
	k_1 (min^{-1})	q_e (mg/g)	R^2	k_2 (g/(mg min))	q_e (mg/g)	R^2
Fe_{Cl}/C (1:4–900)	0.33	6.82	0.991	0.108	7.06	0.999
Fe_N/C (1:4–900)	0.032	15.61	0.990	1.44×10^{-3}	20.24	0.979

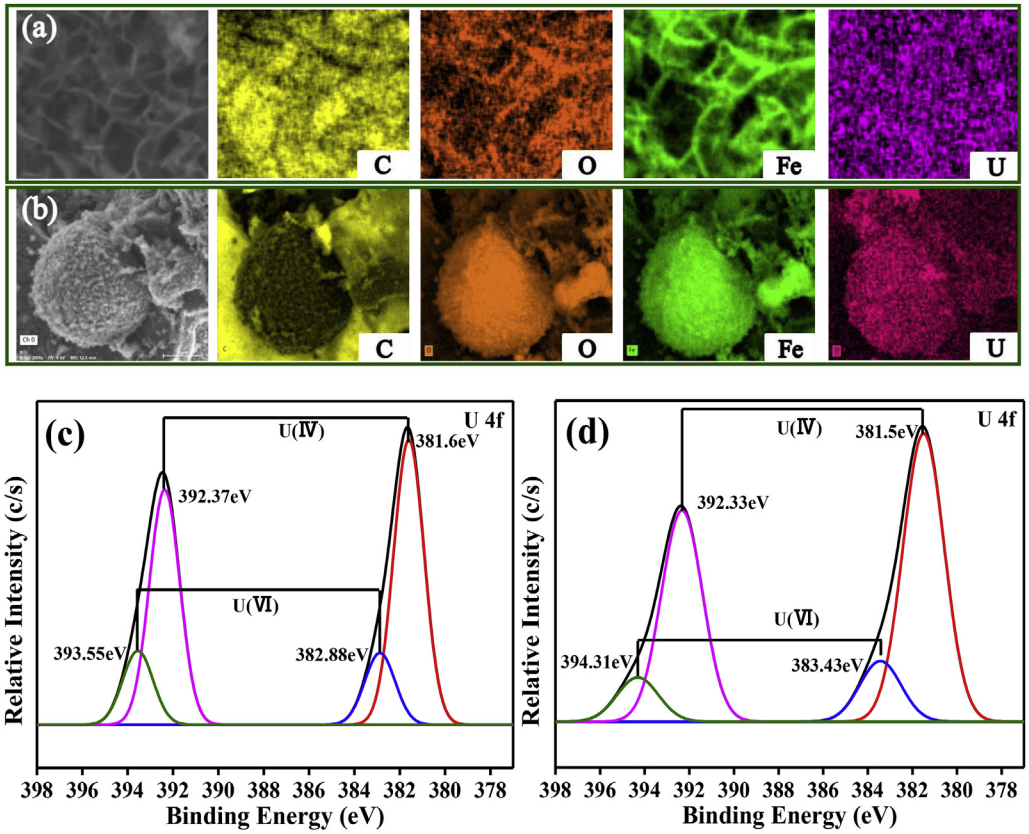


Fig. 6. SEM-mapping of (a) Fe_{Cl}/C (1:4–900); (b) Fe_N/C (1:4–900) and XPS spectra of (c) Fe_{Cl}/C (1:4–900); (d) Fe_N/C (1:4–900) after adsorption of U(VI).

adsorption (Fig. 1(a)), which was due to the contact of U(VI) with ZVI. Similarly, the surface of Fe_N/C (1:4–900) nanoparticles became rough, which may be caused by a new product. Simultaneously, the SEM-mapping of each element (C, O, U, Fe) in Fe_{Cl}/C (1:4–900) and Fe_N/C (1:4–900) after adsorption were displayed in Fig. 6(a) and (b). Exhilaratingly, U was appeared in both Fe_{Cl}/C (1:4–900) and Fe_N/C (1:4–900) after adsorption, which indicated that U(VI) was effectively immobilized. The XPS narrow spectral (Fig. 6(c and d)) of U 4f in Fe_{Cl}/C (1:4–900) and Fe_N/C (1:4–900) were distinctly displayed, from which U(VI) located at 393.55 and 382.88 eV and more apparent U(IV) peaks appeared at 392.37 and 381.6 eV after uranium adsorption on Fe_{Cl}/C (1:4–900). Equally, the U(VI) peak situated at 394.31 and 383.43 eV was weaker than that U(IV) fixed at 392.33 and 381.5 eV for Fe_N/C (1:4–900) after adsorption. To sum up, U(VI) was reduced into U(IV) by ZVI/C (Liu et al., 2017).

4. Conclusion

ZVI/Cs was successfully prepared by carbothermal reduction process. The chloride and ferric nitrate were converted into iron oxides at 700 °C, further being converted into ZVI at 800 and 900 °C. ZVI in the Fe_{Cl}/C (1:4–900) and Fe_N/C (1:4–900) showed the morphology of nanosheets and nanoparticles, respectively. The maximum adsorption capacities of Fe_{Cl}/C (1:4–900) and Fe_N/C (1:4–900) were 34.82 and 55.14 mg/g fitted well with Langmuir isotherm model. Adsorption capacities of oxidized Fe_{Cl}/C (1:4–900) and Fe_N/C (1:4–900) were decreased. The simultaneous presence of U(IV) and U(VI) in the XPS spectra after adsorption indicated simultaneous reduction and adsorption of uranium on Fe_{Cl}/C (1:4–900) and Fe_N/C (1:4–900).

Acknowledgements

This work was supported by the National Natural Science Foundation of China (21976042, U1501231), The Project of Guangdong Provincial Key Laboratory of radioactive contamination control and resources (2017B030314182); Guangdong Provincial Natural Science Foundation (2016A030310265), the Science and Technology Research Programs of Guangzhou City (201804020072), University's 2017 training program for young top-notch personnels (BJ201706). Guangdong Province Universities and Colleges Pearl River Scholar Funded Scheme (2018).

Appendix A. Supplementary data

Supplementary data to this article can be found online at https://doi.org/10.1016/j.jclepro.2019.117873.

References

Cantrell, K.J., Kaplan, D.I., Wietsma, T.W., 1995. Zero-valent iron for the in situ remediation of selected metals in groundwater. J. Hazard Mater. 42 (2), 201–212.
Crane, R.A., Dickinson, M., Popescu, I.C., Scott, T.B., 2011. Magnetite and zero-valent iron nanoparticles for the remediation of uranium contaminated environmental water. Water Res. 45 (9), 2931–2942.
Chen, W., Hsu, C., Du, S., 2015. Thermodynamic analysis of the partial oxidation of coke oven gas for indirect redu of iron oxides in a blast furnace. Energy 86, 758–771.
Chen, L., Feng, S., Zhao, D., Chen, S., Li, F., Chen, C., 2017. Efficient sorption and reduction of U(VI) on zero-valent iron-polyaniline-graphene aerogel ternary composite. J. Colloid Interface Sci. 490, 197–206.
Diao, Z., Xu, X., Jiang, D., Kong, L., Sun, Y., Hu, Y., Hao, Q., Chen, H., 2016. Bentonite-supported nanoscale zero-valent iron/persulfate system for the simultaneous removal of Cr (VI) and phenol from aqueous solutions. Chem. Eng. J. 302, 213–222.
Han, M., Kong, L., Hu, X., Chen, D., Xiong, X., Zhang, H., Su, M., Diao, Z., Ruan, Y., 2018. Phase migration and transformation of uranium in mineralized immobilization by wasted bio-hydroxyapatite. J. Clean. Prod. 197, 886–894.
Hu, B., Guo, X., Zheng, C., Song, G., Chen, D., Zhu, Y., Song, X., Sun, Y., 2019. Plasma-enhanced amidoxime/magnetic graphene oxide for efficient enrichment of U (VI) investigated by EXAFS and modeling techniques. Chem. Eng. J. 357, 66–74.
Huang, S.Y., Jiang, S.B., Pang, H.W., Wen, T., Asiri, A.M., Alamry, K.A., Alsaedi, A., Wang, X.K., Wang, S.H., 2019. Dual functional nanocomposites of magnetic $MnFe_2O_4$ and fluorescent carbon dots for efficient U(VI) removal. Chem. Eng. J. 368, 941–950.
Jing, C., Li, Y., Cui, R., Xu, J., 2015. Illite-supported nanoscale zero-valent iron for removal of 238 U from aqueous solution: characterization, reactivity and mechanism. J. Radioanal. Nucl. Chem. 304 (2), 859–865.
Kong, L., Zhu, Y., Liu, M., Chang, X., Xiong, Y., Chen, D., 2016. Conversion of Fe-rich waste sludge into nano-flake Fe-SC hybrid Fenton-like catalyst for degradation of AOII. Environ. Pollut. 216, 568–574.
Kong, L., Zhang, H., Shih, K., Su, M., Diao, Z., Long, J., Hou, L., Song, G., Chen, D., 2018. Synthesis of FC-supported Fe through a carbothermal process for immobilizing uranium. J. Hazard Mater. 357, 168–174.
Li, J., Chen, C., Zhang, R., Wang, X., 2015. Nanoscale zero-valent iron particles supported on reduced graphene oxides by using a plasma technique and their application for removal of heavy-metal ions. Chem. Asian J. 10 (6), 1410–1417.
Li, J., Wu, Z., Duan, Q., Alsaedi, A., Hayat, T., Chen, C., 2018. Decoration of ZIF-8 on polypyrrole nanotubes for highly efficient and selective capture of U (VI). J. Clean. Prod. 204, 896–905.
Liu, H., Li, M., Chen, T., Chen, C., Alharbi, N.S., Hayat, T., Chen, D., Zhang, Q., Sun, Y., 2017. New synthesis of nZVI/C composites as an efficient adsorbent for the uptake of U (VI) from aqueous solutions. Environ. Sci. Technol. 51 (16), 9227–9234.
Liu, D., Liu, Z., Wang, C., Lai, Y., 2016. Removal of uranium (VI) from aqueous solution using nanoscale zero-valent iron supported on activated charcoal. J. Radioanal. Nucl. Chem. 310 (3), 1131–1137.
Ling, L., Zhang, W., 2015. Enrichment and encapsulation of uranium with iron nanoparticle. J. Am. Chem. Soc. 137 (8), 2788–2791.
Ling, L., Pan, B., Zhang, W., 2015. Removal of selenium from water with nanoscale zero-valent iron: mechanisms of intraparticle reduction of Se (IV). Water Res. 71, 274–281.
Lv, Z., Yang, S., Chen, L., Alsaedi, A., Hayat, T., Chen, C., 2019. Nanoscale zero-valent iron/magnetite carbon composites for highly efficient immobilization of U (VI). J. Environ. Sci. 76, 377–387.
Mangal, H., Saxena, A., Rawat, A.S., Kumar, V., Rai, P.K., Datta, M., 2013. Adsorption of nitrobenzene on zero valent iron loaded metal oxide nanoparticles under static conditions. Microporous Mesoporous Mater. 168, 247–256.
Messele, S.A., Soares, O.S.G.P., Órfão, J.J.M., Stüber, F., Bengoa, C., Fortuny, A., Fabregat, A., Font, J., 2014. Zero-valent iron supported on nitrogen-containing activated carbon for catalytic wet peroxide oxidation of phenol. Appl. Catal. B Environ. 154, 329–338.
Misaelides, P., Godelitsas, A., Filippidis, A., Charistos, D., Anousis, I., 1995. Thorium and uranium uptake by natural zeolitic materials. Sci. Total Environ. 173, 237–246.
Phenrat, T., Saleh, N., Sirk, K., Tilton, R.D., Lowry, G.V., 2007. Aggregation and sedimentation of aqueous nanoscale zerovalent iron dispersions. Environ. Sci. Technol. 41 (1), 284–290.
Qiu, X., Fang, Z., Liang, B., Gu, F., Xu, Z., 2011. Degradation of decabromodiphenyl ether by nano zero-valent iron immobilized in mesoporous silica microspheres. J. Hazard Mater. 193, 70–81.
Qian, Q., Machida, M., Tatsumoto, H., 2007. Preparation of activated carbons from cattle-manure compost by zinc chloride activation. Bioresour. Technol. 98 (2), 353–360.
Qian, L., Ma, M., Cheng, D., 2015. Adsorption and desorption of uranium on nano goethite and nano alumina. J. Radioanal. Nucl. Chem. 303 (1), 161–170.
Ryu, A., Jeong, S.W., Jang, A., Choi, H., 2011. Reduction of highly concentrated nitrate using nanoscale zero-valent iron: effects of aggregation and catalyst on reactivity. Appl. Catal. B Environ. 105 (1–2), 128–135.
Sun, Y., Ding, C., Cheng, W., Wang, X., 2014. Simultaneous adsorption and reduction of U (VI) on reduced graphene oxide-supported nanoscale zerovalent iron. J. Hazard Mater. 280, 399–408.
Song, W., Liu, M., Hu, R., Tan, X., Li, J., 2014. Water-soluble polyacrylamide coated-Fe3O4 magnetic composites for high-efficient enrichment of U (VI) from radioactive wastewater. Chem. Eng. J. 246, 268–276.
Wang, M., Cheng, W., Wan, T., Hu, B., Zhu, Y., Song, X., Sun, Y., 2019. Mechanistic investigation of U (VI) sequestration by zero-valent iron/activated carbon composites. Chem. Eng. J. 362, 99–106.
Wang, X., Chen, L., Wang, L., Fan, Q., Pan, D., Li, J., Chi, F., Xie, Y., Yu, S., Xiao, C., Luo, F., Wang, J., Wang, X., Chen, C., Wu, W., Shi, W., Wang, S., Wang, X., 2019. Synthesis of novel nanomaterials and their application in efficient removal of radionuclides. Sci. China Chem. 62, 933–967.
Wu, X.M., Huang, Q.X., Mao, Y., Wang, X.X., Wang, Y.Y., Hu, Q.H., Wang, H.Q., Wang, X.K., 2019. Sensors for determination of uranium A review. Trends Anal. Chem. 118, 89–111.
Wu, Y.H., Pang, H.W., Liu, Y., Wang, X.X., Yu, S.J., Fu, D., Chen, J.R., Wang, X.K., 2019. Environmental remediation of heavy metal ions by novel-nanomaterials A review. Environ. Pollut. 246, 608–620.
Xie, Y., Chen, C.L., Ren, X.M., Wang, X.X., Wang, H.Y., Wang, X.K., 2019a. Emerging natural and tailored materials for uranium-contaminated water treatment and environmental remediation. Prog. Mater. Sci. 103, 180–234.
Xie, Y., Chen, C.L., Ren, X., Tan, X., Song, G., Chen, D., Alsaedi, A., Hayat, T., 2019b. Coupling g-C_3N_4 nanosheets with metal-organic frameworks as 2D/3D

composite for the synergetic removal of uranyl ions from aqueous solution. J. Colloid Interface Sci. 550, 117–127.
Yan, J., Han, L., Gao, W., Xue, S., Chen, M., 2015. Biochar supported nanoscale zerovalent iron composite used as persulfate activator for removing trichloroethylene. Bioresour. Technol. 175, 269–274.
Yang, D., Wang, X., Wang, N., Zhao, G., Song, G., Chen, D., Liang, Y., Wen, T., Wang, H., Hayat, T., Alsaedi, A., Wang, X., Wang, S., 2018. In-situ growth of hierarchical layered double hydroxide on polydopamine-encapsulated hollow Fe_3O_4 microspheres for efficient removal and recovery of U (VI). J. Clean. Prod. 172, 2033–2044.
Zhang, X., Lin, S., Lu, X., Chen, Z., 2010. Removal of Pb(II) from water using synthesized kaolin supported nanoscale zero-valent iron. Chem. Eng. J. 163 (3), 243–248.
Zhu, K., Chen, C., Xu, M., Chen, K., Tan, X., Wakeel, M., Alharbi, N.S., 2018. In situ carbothermal reduction synthesis of Fe nanocrystals embedded into N-doped carbon nanospheres for highly efficient U (VI) adsorption and reduction. Chem. Eng. J. 331, 395–405.